REMOTE SENSING OF ATMOSPHERE, HYDROSPHERE, AND UNDERLYING SURFACE

Structure of Aerosol Fields of the Atmospheric Boundary Layer according to Aerosol and Doppler Lidar Data During Passage of Atmospheric Fronts

**G. P. Kokhanenko*, Yu. S. Balin, M. G. Klemasheva, I. E. Penner, S. V. Samoilova,
S. A. Terpugova, V. A. Banakh, I. N. Smalikho, A. V. Falits, T. M. Rasskazchikova,
P. N. Antokhin, M. Yu. Arshinov, B. D. Belan, and S. B. Belan**

V.E. Zuev Institute of Atmospheric Optics, Siberian Branch, Russian Academy of Sciences, Tomsk, 634055 Russia

*e-mail: kokh@iao.ru

Abstract—The paper presents the results of complex observations of the atmospheric boundary layer dynamics performed at the Fonovaya Observatory of the Institute of Atmospheric Optics, Siberian Branch, Russian Academy of Sciences, in September 2013, with the use of remote sensing facilities, i.e., aerosol and Doppler lidars. The structure of aerosol and wind fields in the period of occurrence of internal buoyancy waves and low-level jet streams in the boundary layer is considered.

INTRODUCTION

Atmospheric studies especially concentrate on the planetary (or atmospheric) boundary layer (ABL), adjoining the Earth's surface and directly experiencing its effects [1, 2]. The atmospheric dynamics inside the ABL is caused not only by interaction of moving atmospheric masses with an inhomogeneous surface, but also by diurnal cycles, associated with daytime heating of the surface and development of convective mixing. Change of air masses determines the sizes of the atmospheric inhomogeneities spanning from a few to several tens of kilometers corresponding to the mesoscale. In classic textbooks [1–4], as well as in most works in which lidar methods were used to study the structure of the boundary layer [5–9], it was assumed that the structure of the atmosphere on smaller scales (microscales measuring from one hundred meters to a kilometer) is determined by random turbulent mixing. This is also true for convective flow, considered as a set of eddies with the scale of the order of the ABL height, growing with surface warming [9–11].

However, inside the ABL on microscales, there are also regular structures with the formation mechanism associated with buoyancy waves (or, in other words, internal gravity waves, IGWs). These waves are one of the most general phenomena observed in the atmosphere [12]. The IGW structures on different scales (from hundreds of meters to kilometers) may have periods from minutes to hours [13, 14]. They are regularly observed in acoustic [14–16] and laser [5, 17–20] sensing within the ABL. These waves may serve a manifestation of dynamical instability of the atmosphere, produced by strong vertical wind shear on the boundary of the stable layer, and may propagate along this boundary. The necessary condition for IGW occurrence is a shear in wind speed and direction at the boundary of the stable layer.

Micro- and mesoscale phenomena are invariably manifested in the structure of aerosol fields as well. In many cases, aerosol can be considered as a passive tracer, totally entrained by horizontal and vertical flows. Aerosol lidars (lidars that record only elastic backscattering at unshifted wavelengths) allow the observer to trace the structures of aerosol distribution in the ABL (and above), because the signal is adjusted to the square of the distance and is proportional to the aerosol backscattering coefficient β_π. If the aerosol microstructure remains constant during the experiment, β_π can be considered to be proportional to aerosol volume concentration. Therefore, the lidar-observed structure of the aerosol field can be used to visualize the atmospheric stratification and different atmospheric motions.

IGW observations make it possible to detect deviations from atmospheric stratification, generally stable, and, as such, are an important subject of research. A detailed study of the vertical structure of IGW had first been possible with the advent of radars, followed by acoustic and laser radars. It is noteworthy that most valuable results are provided by complex observations,

accompanied by acquisition of information on atmospheric meteorological parameters, such as temperature and wind speed and direction at the time of occurrence of microscale atmospheric structures. In this regard, a large volume of information is produced by Doppler lidars measuring the velocity of aerosol particles [9, 21, 22].

The purpose of this work was to study the processes determining the structure of the aerosol field during passage of IGWs, caused by wind shear at the ABL boundary during passage of an atmospheric front. In the paper, we present measurements of diurnal dynamics of the vertical structure of the ABL by the example of observations on September 25, 2013, when three atmospheric fronts had passed through the observation point during the day. Studies were performed in the framework of the complex experiment, conducted every year at the Fonovaya Observatory of the Institute of Atmospheric Optics, Siberian Branch, Russian Academy of Sciences [23, 24] in Tomsk (near Akademgorodok). The observations (the structure of aerosol layers and wind speed and direction) were based on remote sensing data, obtained with aerosol and Doppler lidars. The vertical profiles of meteorological parameters were measured by launching balloon-sondes, an ultrasonic meteorological station used in ground-based observations. We used the data on the vertical component of the wind velocity in the ABL, obtained using acoustic radar. See section 1 for a more detailed description of the instrumentation. The general structure of the data obtained, including the synoptic situation on the day of observations, is presented in section 2. Section 3 analyzes episodes associated with the occurrence of IGWs in the boundary layer.

1. INSTRUMENTATION AND METHODS OF STUDY

1.1. Aerosol Lidar

The aerosol stratification was studied using multi-wavelength aerosol-Raman lidar "LOZA-S", described in [25, 26]. In this study, we used only the channel of elastic scattering at a wavelength of 1064 nm, because molecular scattering contribution is negligibly small in the IR range and there is a large contrast of aerosol structures.

The lidar is based on a Nd:YAG laser LS-2137U of LOTI TII firm and a mirror Cassegrain receiving telescope with diameter of 300 mm.

The main parameters of the "LOZA-S" lidar are as follows.

Energy per pulse at 1064 nm	700 mJ
Pulse duration	10−12 ns
Pulse repetition rate	10 Hz
Divergence	0.2 mrad

Diameter of main telescope	300 mm
Focal length	1500 mm
Diameter of near-field telescope	40 mm
Focal length	200 mm
Field of view of telescopes	0.8−1 mrad
Sampling rate	25 MHz
ADC capacity	12

Data after digitization were smoothed using 3.2 s temporal and 12 m spatial averaging. The lidar comprises two telescopes for alternate signal reception from near-field (from 20 to 1000 m) and far-field (from 600 m and farther) zones. In processing, signals are sewn at the level of 800−900 m, making it possible to cover a large dynamic variability range of lidar signals in atmospheric sensing. The geometrical function of the near-field receiver is taken into account in signal processing in the range of minimal heights from 40 to 100 m. The method was considered in more detail in work [26]. In the figures, presented in this paper, the structure of the aerosol field is represented using the range-squared-corrected lidar signal, expressed (on conventional color scale) in units of the backscattering ratio, i.e., the ratio of the total (aerosol β_π^a plus molecular β_π^m) backscattering to molecular backscattering: $R_{bs} = (\beta_\pi^a + \beta_\pi^m)/\beta_\pi^m$. Of course, the extinction coefficient of aerosol medium cannot be determined from measurements at a single wavelength. Therefore, the retrieved ratio R_{bs} does not account for the attenuation of scattered light in the atmosphere, and the quantitative value of attenuation is inaccurate (this is the so-called attenuated backscattering ratio). The R_{bs} calibration was performed using the lidar return from the height $H^* = 5−7$ km, where a minimum of aerosol concentration is usually observed; for this, we assumed that $R_{bs}(H^*) = 1.1 \pm 0.4$ [27].

1.2. Doppler Lidar

In the experiment, we employed the pulsed coherent Doppler lidar Stream Line (developed and manufactured by HALO Photonics [28]). In measurements with this lidar, we used conical scanning by sensing beam, which allowed us to obtain information on wind speed and direction from initial lidar data. The elevation angle (i.e., minimal angle between horizontal plane at the lidar level and sensing beam axis) was specified to be 45°. One full conical scanning (with the azimuth angle varying from 0 to 360°) was performed for about 5 min. It is noteworthy that the position of the sensing beam axis was fixed every 3° and a coherent reception of lidar return was performed for 1 s by accumulating data obtained during this time interval (according to parameters, presented below, 15000 sensing pulses sent into the atmosphere were used for the accumulation). The accumulated data with a step of 30 m in range (21.2 m in altitude) were used to esti-

mate the radial velocity (projection of wind velocity onto sensing beam axis). With 3° resolution in azimuth angle, one full conical scanning resulted in 120 altitude profiles of radial velocity estimates. Therefore, total time required to receive the lidar return was 2 min, and about 3 min was spent to change the position of the sensing beam axis (when no reception was performed). The above-described sensing procedure was sequentially applied in a continuous mode from 08:00 to 23:00 Local Time (LT) on September 25, 2013.

The main parameters of Stream Line lidar are as follows.

Wavelength	1500 nm
Energy per pulse	14 μJ
Pulse duration	170 ns
Pulse repetition rate	15 kHz
Telescope diameter	75 mm
Beam radius at telescope exit	20 mm
Focal length	≥300 m
Minimal measurement range	100 m
Maximal measurement range	500−2000 m
Receiver passband	50 MHz

Analysis of radial velocity datasets, obtained in this experiment, showed that the radial velocity estimates are unbiased up to a height of about 600 m, and that the standard procedure of the least-squares method (the so-called sine wave fitting) can be applied to these velocity estimates to obtain information about wind speed and direction. However, above the 600-m level, owing to a very low signal-to-noise ratio, the probability of a bad radial velocity estimate (an estimate, which may take any values within receiver passband, independent of the true radial wind velocity) becomes nonzero. Therefore, the altitude profiles of wind speed and direction were retrieved applying the method of filtered sine wave fitting [29, 30], capable of minimizing the effect of bad estimates on the final result. The application of this method had made it possible to increase the maximal height of wind profile retrievals by 30% as compared to the standard processing procedure.

The "LOZA-S" and Stream Line lidars were installed on the roof of building of the Institute of Atmospheric Optics (15 m above the ground) 40 m apart. It should be remembered that, when Doppler lidar operates in conical scanning mode with the angle 45°, it averages the obtained data over a large scattering volume, the horizontal extent of which is comparable to the sensing altitude. Therefore, the retrieved values of horizontal wind speed and direction are markedly smoothed out and the fine temporal structure of inhomogeneities (on the scales of the period of internal waves) is not processed at high altitudes.

The RS92-SGP Vaisala radiosondes were used to obtain information about the altitude profiles of mete-orological parameters [31]. Helium-filled balloons for radio sensing were launched from the ground near the Lidar Station of the Institute of Atmospheric Optics, at approximately 430 m from the location of the lidars. Sondes were launched every 6 h and ascended at a speed of about 5 m/s. In addition, ultrasonic meteorological station "Meteo-2", developed in the Institute of Atmospheric Optics, Siberian Branch, Russian Academy of Sciences, was used to measure the meteorological parameters at the location of the radars [32].

2. GENERAL PATTERN OF OBSERVATIONS ON SEPTEMBER 25

The state of the atmosphere in the period of observations will be analyzed using a continuous (from 03:00 to 24:00 LT) record of aerosol (Fig. 1a) and Doppler (Fig. 2) lidars, data of synoptic analysis at the 500-mbar level (Fig. 3) and at the near-ground level (Fig. 4), and maps of back trajectories (Fig. 5), calculated according to HYSPLIT model [33, 34]. The radiosonde-derived vertical profiles of wind direction for the study period are presented in Fig. 6. Data of measurements from the ultrasonic meteorological station at lidar height are presented in Fig. 1b (temperature T and pressure P) and Fig. 1c (wind speed V and direction D). The pressure decreases in the first half-day and increases in the second. Wind is moderate and slowly changes from south to north during observations. The temperature behaves in accordance with the diurnal cycle and peaks at 15:00 LT; accordingly, the relative humidity changes in antiphase in the range from 70% in the morning to 30% at noon (not shown in the figure). In lidar data (Fig. 1a) we discern a gradual lowering of the tropopause height (upper boundary of cirrus clouds) from 12 500 to 12 000 m. The ABL height is about 1600−1700 m. By 06:00 LT (morning cooling), two separate layers also appear at heights of about 300 and 500 m in addition to a pronounced near-ground layer (150−200 m).

A fragment of the synoptic chart for the 500-mbar level at 06:00 LT (UTC + 6) is presented in Fig. 3. Before the measurement session, considered here, the atmospheric sensing site (indicated by a triangle in Fig. 3) was located in the peripheral zone of the ridge of a vast Asian anticyclone. All layers in the free troposphere throughout Western Siberia were encompassed by near-western air mass transport, confirmed by data of aerologic sensing at World Meteorological Organization (WMO) stations in Novosibirsk and Kolpashevo, as well as by local radiosonde launches (Fig. 6).

From the ring chart for 09:00 LT (03:00 UTC, Fig. 4a) it can be seen that a tropical occluded front passed through Tomsk at that time; this front was poorly defined because a ridge was present in the troposphere over the study region. The air masses within the boundary layer were transported predominantly from a south-south-west direction, which changed to the western direction as the height increased up to the
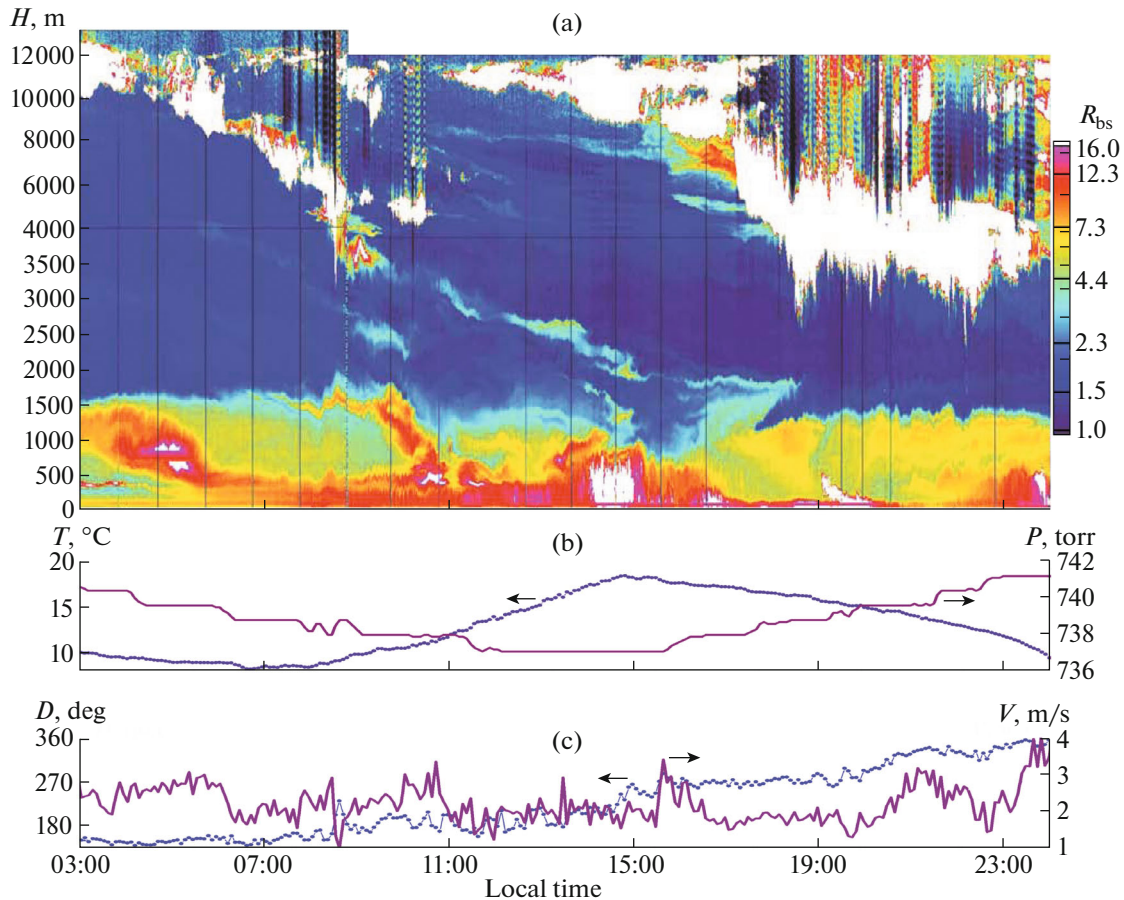
Fig. 1. Vertical structure of aerosol field on September 25, 2013: (a) lidar return at a wavelength of 1064 nm on color scale of back-scattering ratio R_{bs}; and data from meteorological station: (b) temperature T and pressure P; (c) wind speed V and direction D.

level of the free atmosphere (Fig. 6). The wind speeds were minor and stayed within 1−2 m/s; and almost full calm occurred by midday on September 25 (see Fig. 1c), when the region of sensing had been in the col of the pressure systems with unstable and poorly defined frontal divides between western and eastern cyclones and the Arctic and southern anticyclones.

From Fig. 1a (lidar data) it can be seen that the passage of an occluded front is characterized by a rapid descent (starting from 05:00 LT) of cloud layers from the level of cirrus clouds (10 000 m) to a height of 3500 m by 09:00 LT, followed by the occurrence of residual aerosol structures (fog or over-wetted aerosol), merging with near-ground layers (500 m) by 10:00 LT. During rapid descent of the cloud layer in the interval 07:00−08:00 LT there occur pronounced pressure variations within ±0.5 torr with a period of 20 min, accompanied by synchronous oscillations of the height of near-ground layers with an amplitude of ± 50 m. At 08:00 LT, high-frequency IGWs with periods of about 3-5 min occur at the levels of 300- and 500-m stable layers.

Two more fronts passed through the observation point from noon to the morning of the next day. On the ring chart for 03:00 LT on September 26 (Fig. 4b) the polar front is now southward of Tomsk, and the next Arctic front approaches the city. The temperature of near-ground layers on the rear of cold (first polar and then Arctic) fronts decreased in less than a day by 20°: from +22°C at 15:00 LT to +2°C in morning of September 26. It was raining on September 26. During passage of the polar front, the descent of clouds for the second time in the day was apparent in the lidar signal after noon (Fig. 1a) against a background of increasing pressure. Clouds become stable at heights of 3000–3500 m. Simultaneously, an increase in wind speed to 3−4 m/s and a change to a northerly wind regime became apparent by 00:00 LT on September 26 (see Fig. 1c).

A change in the direction of air mass transport during the day at different heights is clearly seen from analysis of back trajectories (Fig. 5, calculated according to HYSPLIT model). Five trajectories are presented in this figure for each level (3000, 1000, and 400 m) with an interval of 4 h, starting from 08:00 UTC (14:00 LT).
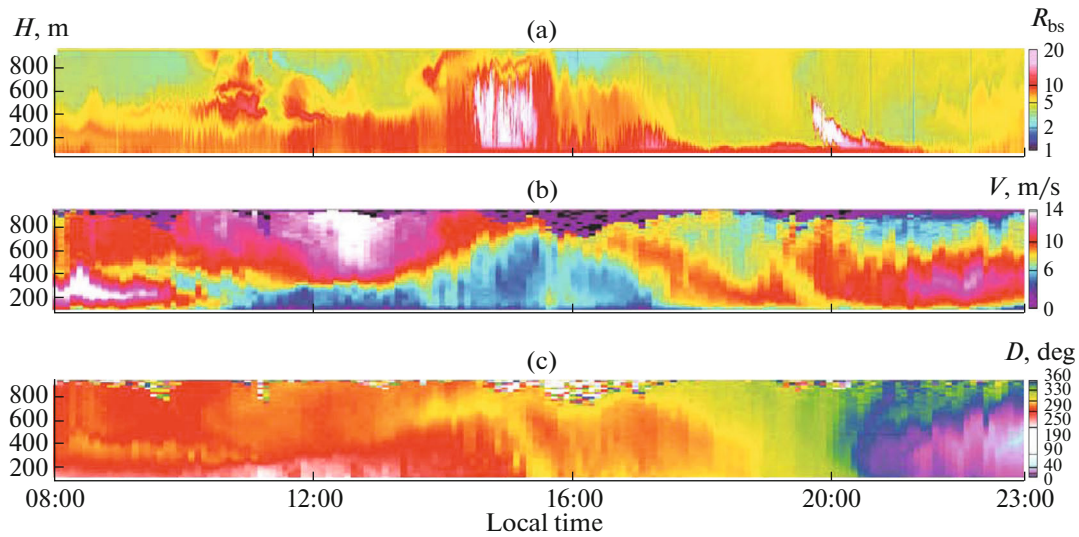
Fig. 2. Simultaneous record of (a) aerosol lidar return and Doppler lidar data: (b) wind speed V and (c) direction D.
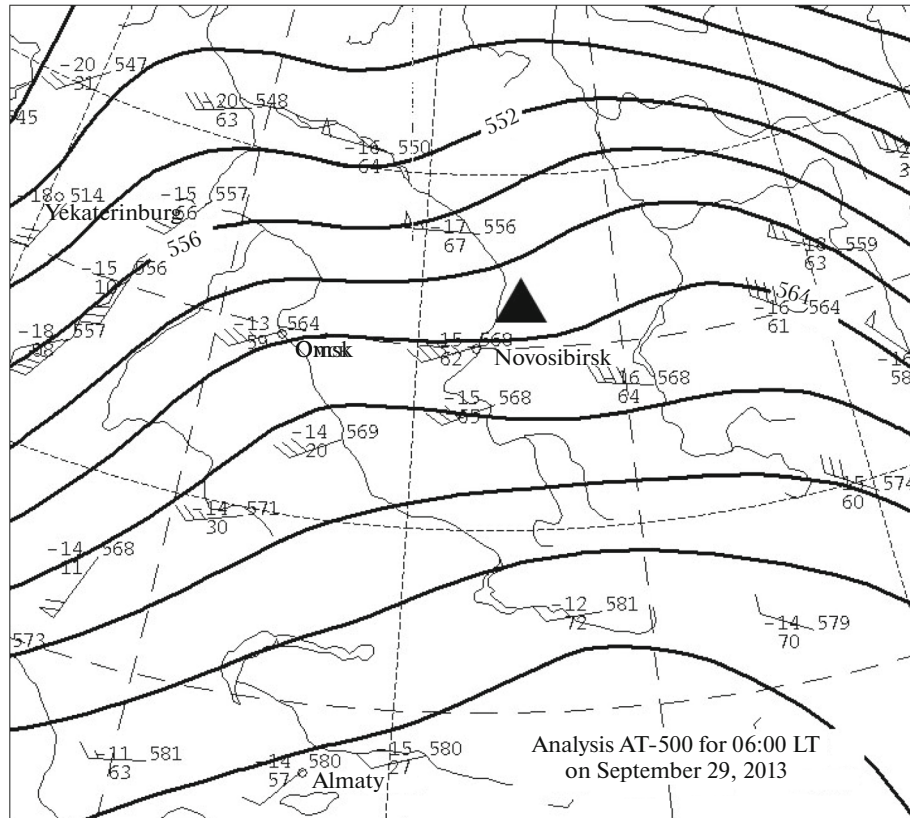
Fig. 3. Synoptic chart at 500-mbar level for 06:00 LT on September 25, 2013.

Whereas almost no change in transport direction occurs for the level of the free atmosphere (3000 m, Fig. 5a), a change from western transport at midday to northern transport toward night is apparent for the level of 1000 m (Fig. 5b). There is a change to the opposite direction of arrival of air masses during the day in the near-ground layers (400 m, Fig. 5c); at the same time, we clearly see that cold Arctic air masses descended (Fig. 5c, lower panel) from the free atmosphere to the boundary layer, which had led to a decrease in the

(a)

(b)
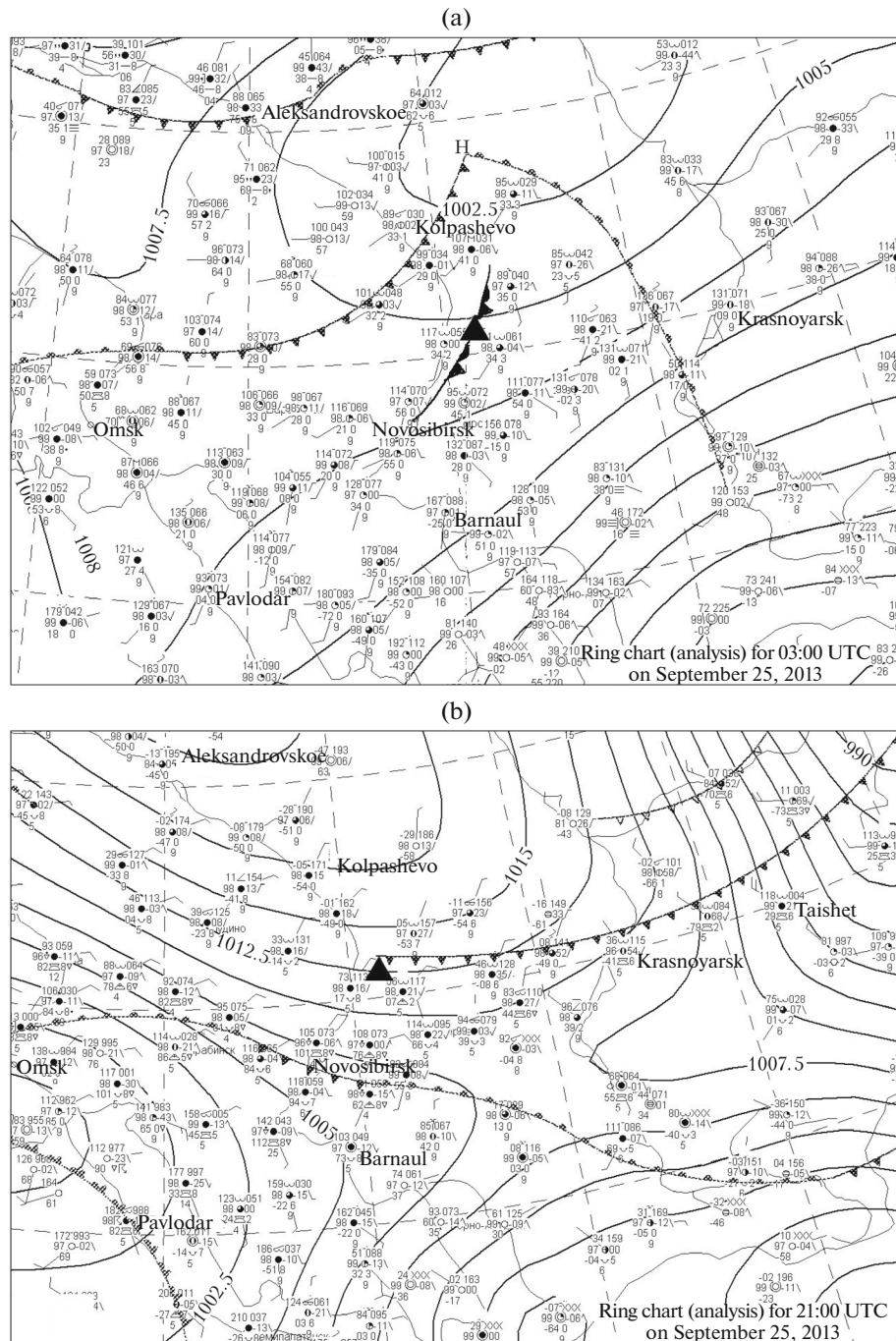
Fig. 4. Ring chart (near-ground analysis) for (a) September 25, 2013, at 09:00 LT (03:00 UTC) and (b) September 26, 2013, at 03:00 LT (21:00 UTC).

near-ground temperature. A change in the wind during the day is also clearly seen from radiosonde measurements (Fig. 6). A change in the wind direction encompasses only lower 1000−1500 m (ABL height), whereas changes in the overlying layer are minor. As a result, a wind shear occurs at the boundary between the ABL and the free troposphere at morning (before 08:00 LT) and evening (after 18:00 LT) hours. From

lidar data, it can be seen that internal waves in the atmospheric boundary layer occur at approximately 20:00 LT.

Figure 2 compares data of aerosol and Doppler lidars for the period from 08:00 to 23:00 LT for the lower 1-km atmospheric layer. Standard meteorological conditions in the boundary (Ekman) layer are characterized by increasing wind speed with height

HOAA HYSPLIT MODEL
Backward trajectories ending at 00:00 UTC 26 Sep 13
GFSC meteorogical data

HOAA HYSPLIT MODEL
Backward trajectories ending at 00:00 UTC 26 Sep 13
GFSC meteorogical data

HOAA HYSPLIT MODEL
Backward trajectories ending at 00:00 UTC 26 Sep 13
GFSC meteorogical data
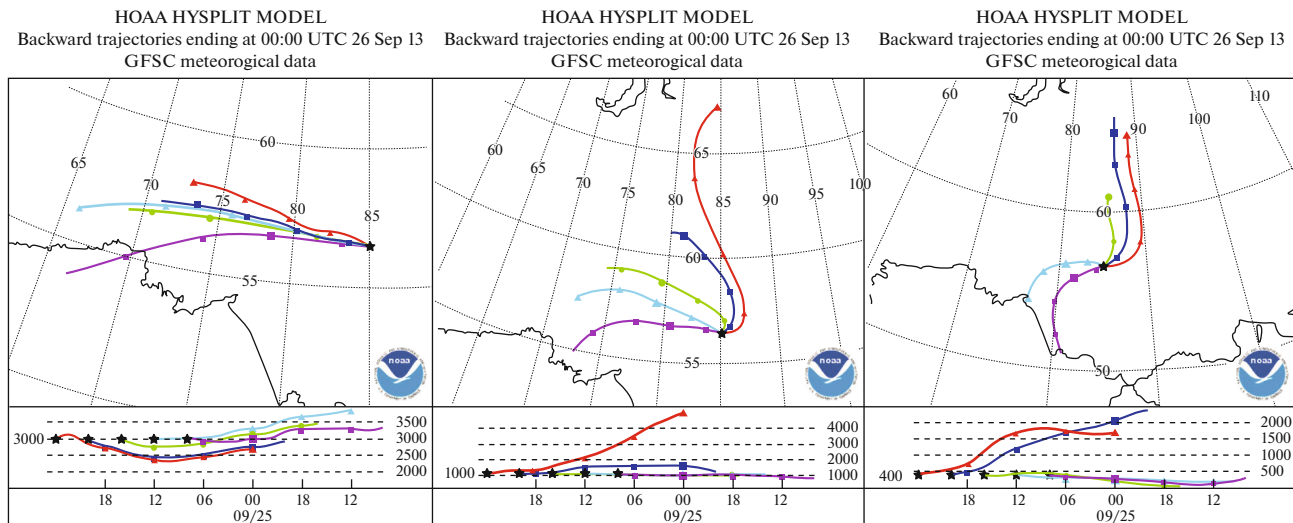
Fig. 5. Map of back trajectories for September 25, 2013, at heights of (a) 3000, (b) 1000, and (c) 400 m.

and a slow veering to the right until coincidence with the geostrophic wind direction [1, 4]. In the given case, the wind shows a more complex pattern, starting to correspond to the above-indicated rule only at midday. In the morning hours (08:00−11:00 LT) at heights of 300−400 m, there is a clearly discernible jet stream, characterized by elevated (to over 14 m/s) wind speed and wind direction turned to the right relative to the underlying layers. Another, more vertically extensive jet stream occurs after 20:00 LT at heights of about 400 m. These time periods, as already indicated above, are associated with a frontal passage and change in wind direction in the boundary layer, accompanied by occurrence of internal waves inside and at the boundary of the ABL. In the next section, we will consider the two time intervals in more detail, employing data on atmospheric stratification and wind profile in the ABL.

3. STRUCTURE OF ATMOSPHERIC LAYERS IN THE PERIOD OF IGW PASSAGE

3.1. Morning Hours on September 25

Figure 7 shows data of Vaisala radiosonde sensing in the layer up to 1400 m; the balloon was launched at 08:30 LT. In Fig. 8, for the same layer, we compare data of aerosol lidar and wind speed and direction, retrieved from the data of the Doppler lidar.

Temperature gradients in the ABL are clearly apparent, with inversions at heights of 150, 300, and 500 m. Local maxima of Väisälä frequency correspond to these boundaries, between which there is near-indifferent stratification. The relative humidity also markedly differs between the near-ground layer (0−150 m) and the layer of 150−300 m, and then decreases even more strongly up to the boundary of the 500-m layer. Wind speed reaches a maximum at a height of

300 m, while the wind veers through maximal angle (at 400 m) between two aerosol layers. As already indicated above (see Fig. 1), around 08:30 LT there were oscillations of near-ground pressure within the range ±0.5 torr with a period of 20 min, accompanied by synchronous oscillations of the height of the mixing layer (500 ± 50) m. From Fig. 8b, it can be seen that at this time the wind speed at the upper boundary of the 300-m layer "strikingly" increases to over 16 m/s. Simultaneously, the jet stream appears at a height of 400 m (at the level between two aerosol layers with the upper boundaries at 300 and 500 m), characterized by wind veering through 70° to the right relative to the near-ground layer, and return veering through 50° to the left above this layer. This instability leads to occurrence of high-frequency IGWs, discernible in the aerosol record at the boundaries of the 300- and 500-m layers. By 09:30 LT, signatures of the near-ground layer (0−150 m) disappear, and oscillations fill all the 300-m mixing layer. Oscillations at the boundary of the 500-m layer exist with the same period and phase, and their effect is traced up to the height of the upper boundary of the intercepting layer at 700 m.

The jet stream exists between two layers until 10:40 LT, and then it breaks down under the impact of descending aerosol (or fog?) layers; accordingly, waves also decay, first in the 500-m layer and then below.

The oscillations are quite synchronous at the boundaries of the 300- and 500-m layers. The period of oscillations is about 3 min, the correlation coefficient between the heights of the waves (determined according to the maximum of backscattering gradient) on a 40-minute time interval of 9:50−10:30 LT (more detailed fragment of lidar record is presented in Fig. 9) is 0.4 for a zero lag of the cross-correlation function. However, the aerosol layers differ in shape. At a height

of 500 m, we clearly see the boundary of the layer, identified from increased backscattering and oscillating with an amplitude of 100−150 m. There is no oscillating boundary at a height of 300 m. Instead, there are periodic vertical structures with increased backscattering ("columns") in phase with the maxima of the wave height and gaps (with decreased backscattering), reaching the near-ground level. Backscattering increases in "columns" by 13−14%. Similar "columns" can also be seen in the mixing layer above the 500-m boundary (this layer gradually grows and reaches the height of 720 m by 10:20 LT); however, the backscattering increases by no more than 7−8% in this region. These structures may originate from alternating upward and downward air motions, encompassing simultaneously the entire mixing layer. To identify these motions, it is useful to consider data on the vertical component of the wind velocity during measurements.

In our experiment, data on vertical wind, obtained with Doppler lidar, had insufficient accuracy and low time resolution in view of the chosen operation mode, with lidar circumscribing a wide cone with a period of 5 min. Therefore, we used the vertical component of the wind velocity, measured with the Doppler sodar "Volna-4". Information on sodar can be found in [35, 36]. The sodar was located near "LOZA-S" lidar at a distance of 10 m; therefore, the volumes, sensed by lidar and sodar, can be considered almost coincident.

Figure 9, on a large scale, presents the lidar record, on which we superimposed the sodar-measured vertical component of wind velocity w (m/s). The figure is borrowed with permission from the author [37], using data previously published in [38]. The $w(t)$ data are averaged over altitudes of the layers indicated in the figure. The wind speed increases with the height of the layer and, most important for our consideration, the upward motion changes to downward motion simultaneously throughout the height of the mixing layer. We should note that the maxima of the vertical wind and wave maxima at the boundary of the mixing layer are substantially (by about 1 min) separated in time. Similar mismatches in acoustic measurements were also observed before [14, 39] for reasons unclear to the authors yet.

The origin of the observed "columns" in zones of updrafts and downdrafts can probably be explained by the well-known dependence of the aerosol scattering coefficient on relative air humidity. The hygroscopicity of particulate material under the background continental atmospheric conditions is known to cause moisture uptake by the particulate material. In most cases, changes in the scattering coefficient can be described by simple empirical dependence of the scattering coefficient μ on the relative humidity f, suggested in works of Kasten [40] and Hanel [41]: $\mu = \mu_d(1 - f)^{-\gamma}$, where μ_d is the scattering coefficient caused by the dry base of particles; and γ is the parameter of condensation activity, which determines the
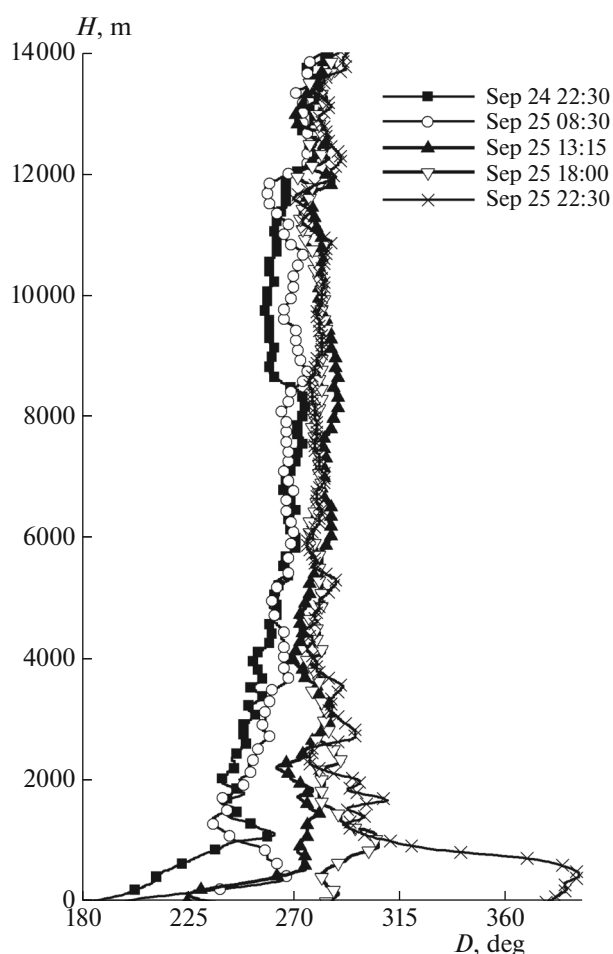
Fig. 6. Changes in the vertical profile of wind direction D during September 24−25, 2013, from radiosonde data (local time).

dynamics of the optical characteristic as a function of humidity. As the relative humidity increases to a certain (critical) value f^*, a phase transition takes place, and the particle is converted to saturated salt solution, leading to a rapid spontaneous growth of particle size [42−44]. A specific f^* value at the critical point may change from 15 to 81%, depending on aerosol chemical composition [45].

The systematic studies of the condensation activity on the territory of western Siberia [46−48] show that the most probable value of the critical relative humidity f^* is 70%, and that the phase transition outside the range of 55−80% is very rare occurrence. At this f^* value, the scattering coefficient μ may increase by 30−70%.

The signal, recorded by laser radar (lidar), is determined by the backscattering coefficient $\beta_\pi = \mu/L$, where L is called the lidar ratio. For a typical atmospheric aerosol, observed by different authors, the L values lie in the range 20−80 sr [49]. Like the scat-
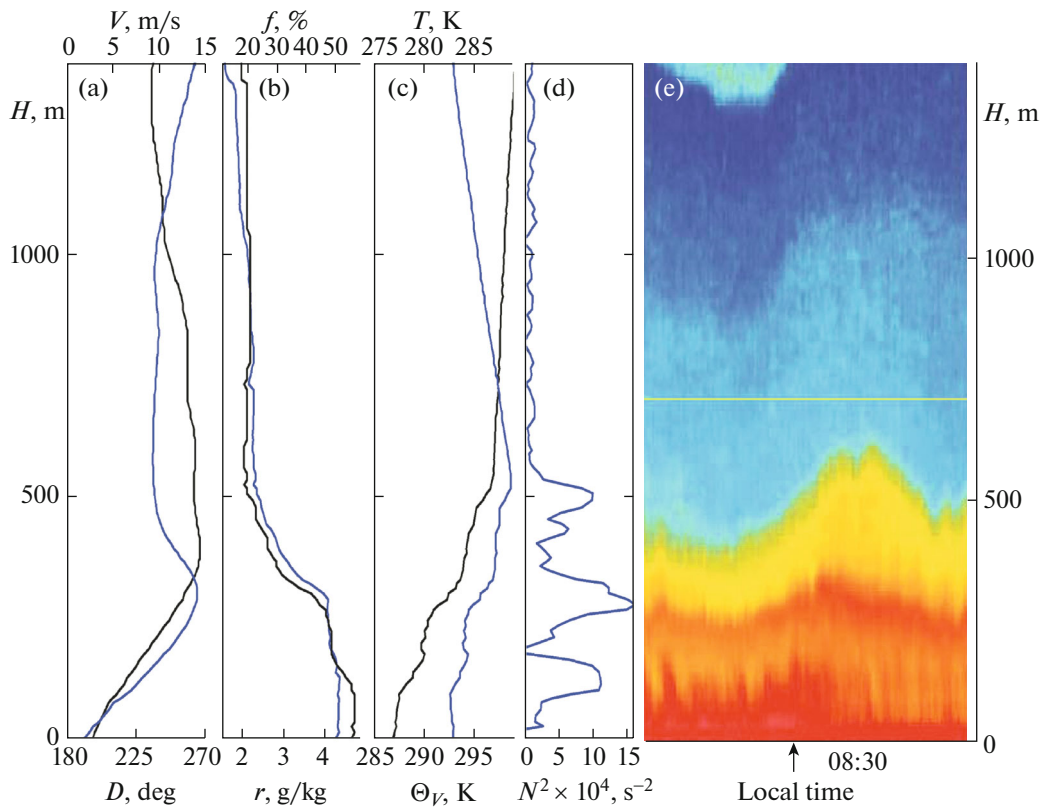
Fig. 7. Radiosonde sensing data (balloon launched at 08:30 LT): (a) wind speed V and direction D; (b) relative humidity f and water vapor mixing ratio r; (c) temperature T and virtual potential temperature Θ_V; (d) Väisälä frequency $N^2 = \dfrac{g}{\Theta}\dfrac{\partial\Theta}{\partial H}$, 1/s²; (e) fragment of aerosol lidar record (time and R_{bs} scales are as in Fig. 8).

tering coefficient μ, the lidar ratio depends on particle size and refractive index of the particulate material, and varies with changes in relative humidity. Calculations [50] and direct measurements [51−53] show that the lidar ratio in many cases either does not depend on the relative humidity [54], or grows more slowly than the scattering coefficient [55, 56]. As a result, the above-mentioned works lead us to conclude that backscattering grows (more or less rapid) with increasing humidity. This behavior is indirectly confirmed by numerous lidar observations of the atmospheric boundary layer, which show a strong correlation between water vapor content (expressed via both relative and specific humidities) and the backscattered signal [21, 24, 30, 54−57]. This effect is especially apparent in observations of thermals in the convective mixing layer [6, 8, 11]: turbulent mixing leads to a gradual air ascent, the relative humidity grows due to adiabatic expansion, and tops of thermals exhibit much larger backscattering than near-ground layers.

Our pattern differs from the usual behavior of the convective boundary layer in that all the layer is affected by a passing IGW. This effect is superposed on turbulent mixing, causing a simultaneous ascent of the layer throughout the height, suggesting that adiabatic cooling and increase in relative humidity take place in the entire layer during air ascent.

The relative humidity $f = e/E(T)$, where e is the partial pressure of water vapor and $E(T)$ is the saturation pressure at temperature T. During adiabatic expansion, e decreases proportionally to the atmospheric pressure P in accordance with the adiabatic equation $T/T_0 = (P/P)^{0.286}$ [4], with temperature T during air ascent to the height H decreasing according to the linear dependence $T = T - \gamma_a H$ ($\gamma_a = 0.98$ °C/100 m is the adiabatic gradient). The saturation pressure E can be calculated from formula [58]: $E(T) = 6.112\exp[17.62T/(243.12 + T)]$, where T is in °C.

The calculation from the formulas above gives an increase in the relative humidity at an initial temperature of 10°C (which is the temperature in the morning hours, see Fig. 1b) by 5.5% during ascent by 100 m, which is the average IGW amplitude in the 500-m layer. At an initial humidity of 60%, the scattering
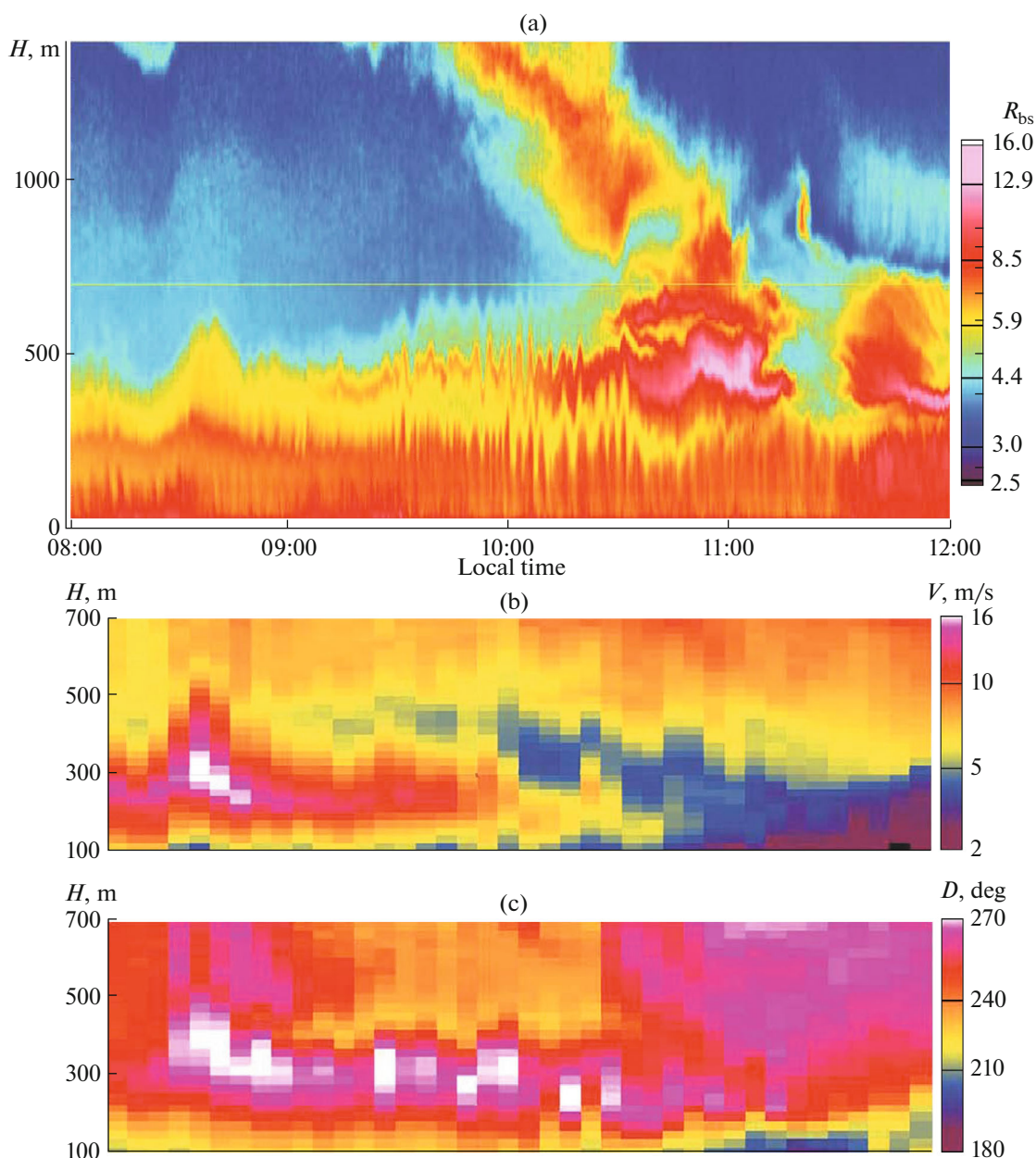
Fig. 8. (a) Record of aerosol lidar returns on R_{bs} scale and (b) wind speed and (c) direction, retrieved from Doppler lidar data.

coefficient in this case (considering the fact that the probable value of the parameter γ for midlatitude air masses is γ = 0.4 [48]) will increase by 4%, less than observed in our measurements. Undoubtedly, an important role in our case is played by phase transition in the particulate material, very probable at a relative humidity of 60% in the lower mixing layer, so that backscattering increases by 10−13% in updrafts. In the upper layer at 500−700 m, the relative humidity is lower (20%), the phase transition at this humidity rare occurs, explaining why scattering in columns increases more weakly, by about 5−7%.

3.2. Atmospheric Dynamics during Evening of September 25

The situation in the period 21:00−00:00 LT is shown in Figs. 10 and 11, where data are presented similarly to Figs. 7 and 8. Figure 10 presents data of Vaisala radiosonde sensing in the layer up to 2500 m; the balloon was launched at 22:30 LT. The lidar record reveals a few aerosol layers, the boundaries of which coincide with local maxima of frequency N^2. These layers are difficult to discern on the potential-temperature profile. A maximum wind speed is observed at a height of 200 m (the lowest mixing layer), as well as veering of wind direction
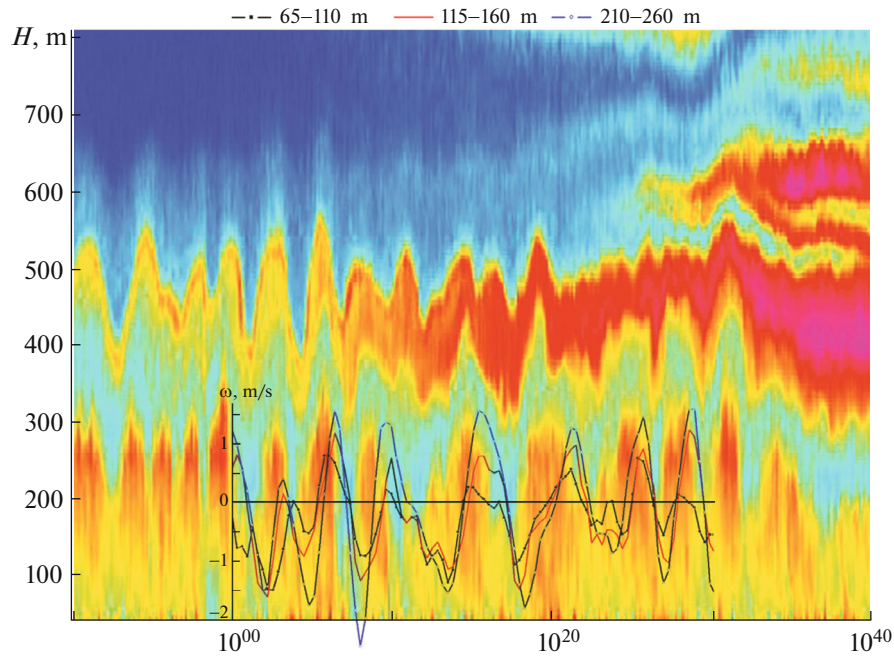
Fig. 9. Fragment of aerosol lidar record, with superimposed vertical component of wind velocity w (m/s), measured with sodar at different heights.
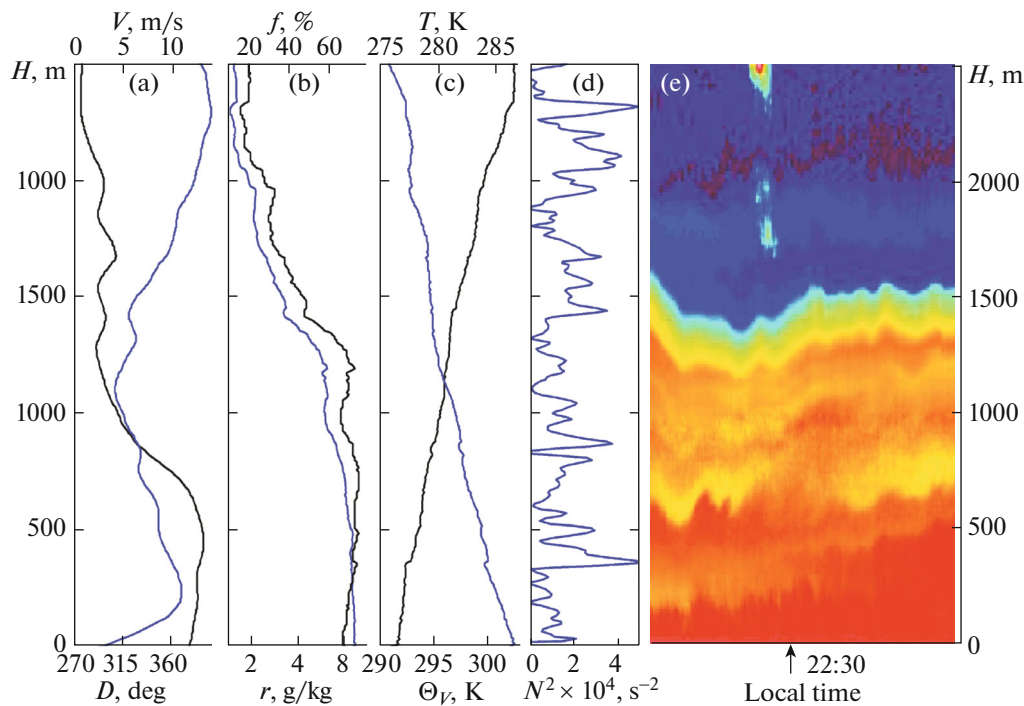
Fig. 10. Radiosonde sensing data (balloon launched at 22:30 LT): (a) wind speed V and direction D; (b) relative humidity f and

water vapor mixing ratio r; (c) temperature T and virtual potential temperature Θ_V; (d) Väisälä frequency $N^2 = \dfrac{g}{\Theta}\dfrac{\partial\Theta}{\partial H}$, 1/s²;

(e) fragment of aerosol lidar record.

to the left at heights from 500 to 1300 m (upper boundary of the ABL).

The water vapor is quite uniformly mixed inside the ABL (see the profile of the mixing ratio $r(H)$ in

Fig. 10b); however, the profile of the relative humidity $f(H)$ exhibits minor maxima (such as at heights of 350, 500, and 1200 m), obviously associated with temperature drops. This, in turn, leads to minor increases of
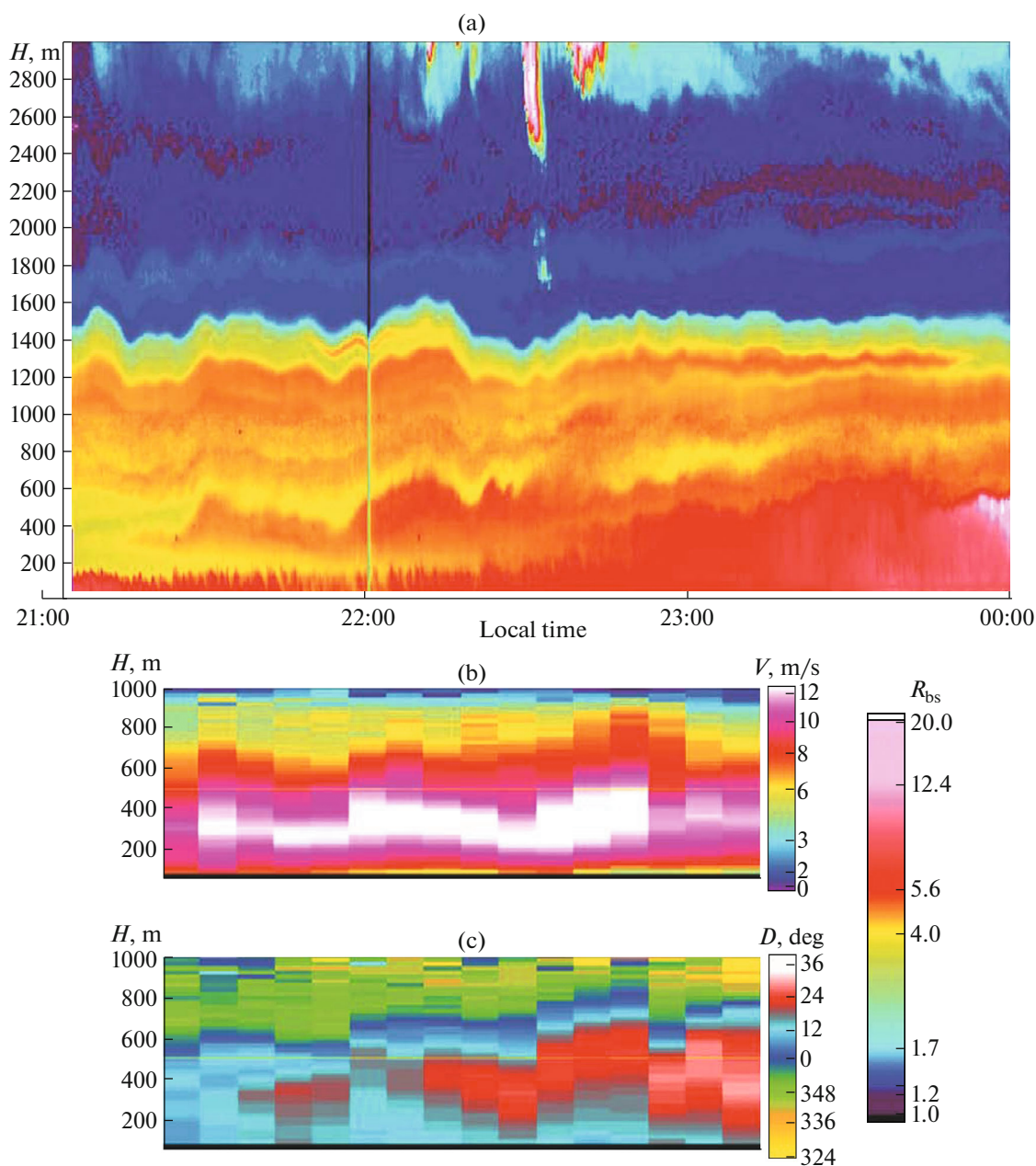
Fig. 11. (a) Aerosol lidar record and (b) wind speed and (c) direction, retrieved from Doppler lidar data.

backscattering at the upper boundaries of the mixing layers, whereby separate layers on the record of aerosol lidar returns are easily discernible (Figs. 10e and 11a). Data of the Doppler lidar (Figs. 11b, 11c) show the presence of jet stream at heights of 300–400 m. The wind speed exceeds 12 m/s in this height interval and decreases to 3 m/s at a height of 900 m. Wind veering to the right relative to the near-ground layer (Fig. 11c) occurs at 22:00 LT, somewhat later than the increase in stream speed; and the wind again veers to the left in overlying layers. This shear of wind speed and direction in the presence of a few stable layers leads to the occurrence of IGWs through the entire ABL depth, starting from the height of the near-ground layer (150 m

at 22:00 LT) to the ABL upper boundary at 1600 m. The most pronounced IGW at 22:10 reaches the amplitude of 200 m and is traced without phase shift up to the aerosol layer at height of 1800 m. At 23:00 LT, the wind speed shear in the jet stream decreases, leading to the elimination of conditions favoring the existence of buoyancy waves and to decay of oscillations at the boundary of the ABL and inside it.

CONCLUSIONS

We presented the results of the complex observations of the atmospheric boundary layer dynamics using remote sensing facilities. Data on scattering

properties of the atmosphere, meteorological parameters, wind speed and direction, obtained simultaneously at different heights with a good time resolution made it possible to comprehensively study the atmospheric boundary layer structure and dynamics, compare the distribution of aerosol layers with data on temperature stratification of the atmosphere, on shear of wind speed and direction at the boundary of stable layers inside ABL, and, in particular, to trace the process of occurrence of internal waves at the boundary of mixing layers.

Two episodes of internal buoyancy waves in the atmospheric boundary layer, presented here, are associated with the passage of a few (tropical and polar) atmospheric fronts through the observation point during the day. It is shown that the reason for IGW origin and persistence had been the occurrence of a low-level jet stream at the boundary of the mixing layer, accompanied by a shear of wind speed and direction. In the morning episode, the synchronous oscillations of the levels of stable layers in the IGW field with a period of about 3 min are traced from the near-ground layer to a height of 700−750 m. In the evening, the jet stream at heights of 300−400 m gave rise to slower waves, encompassing the layer 1800 m in height.

The aerosol layers with enhanced backscattering, present in the ABL, are well explained by specific features of temperature stratification of the atmosphere. At the same time, under the conditions of IGW passage, the structure of lidar-observed aerosol backscattering markedly differs from the pattern of well-mixed turbulent convective layer. Usually, the turbulent flows lead to a complete mixing in the lower part of the convective layer, and only tops of thermals exhibit an elevated backscattering. In the case of IGW passage, air simultaneously ascends through the entire height of the mixing layer, relative humidity increases through the entire ABL height as a result of adiabatic expansion of air masses during upward motion, and, therefore, increases aerosol backscattering. The fact that relative humidity plays quite an important role in the lower mixing layer leads to exceeding the "critical point" of phase transition in the particulate material, explaining why backscattering increases much more strongly (by 10−13%) in the lower layer than in the upper layer above 500 m, where the relative humidity is low and the phase transition has low probability. On the aerosol lidar record, this looks like the appearance of vertical structures ("columns") with height encompassing the entire mixing layer and considerably exceeding the IGW amplitude, existing at the upper boundary of the layer. This pattern, with the appearance of vertical "columns", was also often observed before [38, 59]; but firm conclusions had to await meteorological support.

The results of the work demonstrate that such complex experiments are promising for studying the atmospheric boundary layer structure and variations.

REFERENCES

1. R. B. Stull, *An Introduction to Boundary Layer Meteorology* (Kluwer Academic Publisher, 1988).

2. R. A. Braun, *Analytical Methods for Simulation of the Planetary Boundary Layer* (Gidrometeoizdat, Leningrad, 1978) [in Russian]

3. T. R. Oke, *Boundary Layer Climates* (Taylor & Francis e-Library, 2002).

4. L. T. Matveev, *Course of General Meteorology. Atmospheric Physics* (Gidrometeoizdat, Leningrad, 1984) [in Russian]

5. G. Martucci, R. Matthey, V. Mitev, and H. Richner, "Frequency of boundary-bayer-top fluctuations in convective and stable conditions using laser remote sensing," Bound.-Lay. Meteorol. **135** (2), 313−331 (2010).

6. T. D. Crum, R. B. Stull, and E. W. Eloranta, "Coincident lidar and aircraft observations of entrainment into thermals and mixed layers," J. Climate Appl. Meteorol. **26** (7), 774−788 (1987).

7. E. W. Eloranta and D. K. Forrest, "Volume-imaging lidar observations of the convective structure surrounding the flight path of a flux-measuring aircraft," J. Geophys. Res., D **97** (17), 18383−18393 (1992).

8. S. H. Melfi, J. D. Spinhirne, S-H. Chou, and S. P. Palm, "Lidar observation of vertically organized convection in the planetary boundary layer over the ocean," J. Climate Appl. Meteorol. **24** (8), 806−821 (1985).

9. M. Lothon, D. H. Lenschow, and S. D. Mayor, "Coherence and scale of vertical velocity in the convective boundary layer from a Doppler lidar," Bound.-Lay. Meteorol. **121** (3), 521−536 (2006).

10. K. E. Kunkel, E. W. Eloranta, and S. T. Shipley, "Lidar observations of the convective boundary layer," J. Appl. Meteorol. **16** (12), 1306−1311 (1977).

11. D. Atlas, B. Walter, S. H. Chou, and P. J. Sheu, "The structure of the unstable marine boundary layer viewed by lidar and aircraft observations," J. Atmos. Sci. **43** (13), 1301−1318 (1986).

12. E. E. Gossard and W. Hooke, *Waves in the Atmosphere* (Elsevier, New York, 1975).

13. S. Viana, C. Yague, and G. Maqueda, "Propagation and effects of a mesoscale gravity wave over a weakly-stratified nocturnal boundary layer during the SABLES2006 field campaign," Bound.-Lay. Meteorol. **133** (2), 165−188 (2009).

14. I. Petenko, G. Mastrantonio, A. Viola, S. Argentini, and I. Pietroni, "Wavy vertical motions in the ABL observed

by sodar," Bound.-Lay. Meteorol. **143** (1), 125−141 (2012).

15. S. L. Odintsov, "Peculiarities in motion of the lower atmospheric layer at passage of the internal gravity waves," Atmos. Ocean. Opt. **15** (12), 1026−1030 (2002).

16. V. S. Lyulyukin, R. D. Kuznetsov, and M. A. Kallistratova, "The composite shape and structure of braid patterns in Kelvin−Helmholtz billows observed with a sodar," J. Atmos. Ocean. Technol. **30** (12), 2704−2711 (2013).

17. R. Boers and E. W. Eloranta, "Lidar measurements of the atmospheric entrainment zone and the potential temperature jump across the top of the mixed layer," Bound.-Lay. Meteorol. **34** (4), 357−375 (1986).

18. M. Pahlow, J. Kleissl, M. B. Parlange, J. M. Ondov, and D. Harrison, "Atmospheric boundary-layer structure observed during a haze event due to forest-fire smoke," Bound.-Lay. Meteorol. **114** (1), 53−70 (2005).

19. K. Traumner, Ch. Kottmeier, U. Corsmeier, and A. Wieser, "Convective boundary-layer entrainment: Short review and progress using doppler lidar," Bound.-Lay. Meteorol. **141** (3), 369−391 (2011).

20. D. Lesouef, F. Gheusi, P. Chazette, R. Delmas, and J. Sanak, "Low tropospheric layers over reunion island in lidar-derived observations and a high-resolution model," Bound.-Lay. Meteorol. **149** (3), 425−453 (2013).

21. F. Gibert, J. Cuesta, J.-I. Yano, N. Arnault, and P. H. Flamant, "On the correlation between convective plume updrafts and downdrafts, lidar reflectivity and depolarization ratio," Bound.-Lay. Meteorol. **125** (3), 553−573 (2007).

22. V. A. Banakh, I. N. Smalikho, A. V. Falits, B. D. Belan, M. Yu. Arshinov, and P. N. Antokhin, "Joint radiosonde and Doppler lidar measurements of wind in the atmospheric boundary layer," Atmos. Ocean. Opt. **28** (2), 185-191 (2015).

23. G. G. Matvienko, B. D. Belan, M. V. Panchenko, O. A. Romanovskii, S. M. Sakerin, D. M. Kabanov, S. A. Turchinovich, Y. S. Turchinovich, T. A. Eremina, V. S. Kozlov, S. A. Terpugova, V. V. Pol'kin, E. P. Yausheva, D. G. Chernov, T. B. Zhuravleva, T. V. Bedareva, S. L. Odintsov, V. D. Burlakov, A. V. Nevzorov, M. Y.Arshinov, G. A. Ivlev, D. E. Savkin, A. V. Fofonov, V. A. Gladkikh, A. P. Kamardin, Y. S. Balin, G. P. Kokhanenko, I. E. Penner, S. V. Samoilova, P. N. Antokhin, V. G. Arshinova, D. K. Davydov, A. V. Kozlov, D. A. Pestunov, T. M. Rasskazchikova, D. V. Simonenkov, T. K. Sklyadneva, G. N. Tolmachev, S. B. Belan, V. P. Shmargunov, A. S. Kozlov, and S. B. Malyshkin, "Complex experiment on studying the microphysical, chemical, and optical properties of aerosol particles and estimating the contribution of atmospheric aerosol-to-earth radiation budget," Atmos. Measur. Tech. **8** (10), 4507−4520 (2015).

24. I. E. Penner, Yu. S. Balin, M. V. Makarova, M. Yu. Arshinov, B. A. Voronin, B. D. Belan, S. S. Vasil'chenko, V. I. Serdyukov, L. N. Sinitsa, E. R. Polovtseva, D. M. Kabanov, and G. P. Kokhanenko, "Investigations of total water vapor content using various techniques. Comparison of water vapor and aerosol profiles," Opt. Atmos. Okeana **27** (8), 728−738 (2014).

25. S. V. Samoilova, Yu. S. Balin, G. P. Kokhanenko, and I. E. Penner, "Investigations of the vertical distribution of troposphere aerosol layers based on the data of multi-frequency raman lidar sensing: Part 1. Methods of optical parameter retrieval," Atmos. Ocean. Opt. **22** (3), 302−315 (2009).

26. Yu. S. Balin, G. S. Bairashin, G. P. Kokhanenko, M. G. Klemasheva, I. E. Penner, and S. V. Samoilova, "LOSA-M2 aerosol Raman lidar," Quantum Electron. **41** (10), 945−949 (2011).

27. Z. Tao, M. P. McCormick, D. Wu, Z. Liu, and M. A. Vaughan, "Measurements of cirrus cloud backscatter colour ratio with a two-wavelength lidar," Appl. Opt. **47** (10), 1478−1485 (2008).

28. G. Pearson, F. Davies, and C. Collier, "An analysis of performance of the UFAM pulsed Doppler lidar for the observing the boundary layer," J. Atmos. Ocean. Technol. **26** (2), 240−250 (2009).

29. I. N. Smalikho, "Techniques of wind vector estimation from data measured with a scanning coherent Doppler lidar," J. Atmos. Ocean. Technol. **20** (2), 276−291 (2003).

30. V. A. Banakh, A. Bryuer, E. L. Pichugina, and I. N. Smalikho, "Measurements of wind velocity and direction with coherent Doppler lidar in conditions of a weak echo signal," Atmos. Ocean. Opt. **23** (5), 381−388 (2010).

31. http://www.vaisala.com/en/products/soundingsystem-sandradiosondes/radiosondes/Pages/RS92.aspx

32. V. A. Gladkikh and A. E. Makienko, "Digital ultrasonic weather station," Pribory, No. **7**, 21−25 (2009).

33. A. F. Stein, R. R. Draxler, G. D. Rolph, B. J. B. Stunder, M. D. Cohen, and F. Ngan, "NOAA'S HYSPLIT atmospheric transport and dispersion modeling system," Bull. Amer. Meteorol. Soc. **96** (12), 2059−2077 (2015).

34. G. D. Rolph, Real-time Environmental Applications and Display sYstem (READY). http://www.ready.noaa.gov.

35. V.A. Gladkikh, A.E. Makienko, V.A. Fedorov, "Volna-3 Doppler sodar," Atmos. Ocean. Opt. **12** (5), 422-429 (1999).

36. A. P. Kamardin, G. P. Kokhanenko, I. V. Nevzorova, and I. E. Penner, "Joint lidar and sodar investigations of the atmospheric boundary layers," Opt. Atmos. Okeana **24** (6), 534−537 (2011).

37. A. P. Kamardin, S. L. Odintsov, and A. V. Skorokhodov, "Identification of internal gravity waves in the atmospheric boundary layer from sodar data," Opt. Atmos. Okeana **27** (9), 812−818 (2014).

38. G. P. Kokhanenko and S. A. Terpugova, "Relationship of spatial structure of aerosol and humidity during passage of the internal gravity wave," Proc. SPIE—Int. Soc. Opt. Eng. **9292**, 92923S (2014). doi 10.1117/12.207550310.1117/12.2075503

39. S. Ya. Odintsov, "The study of the atmospheric boundary layers by methods of local and remote acoustic diagnostics at the IAO SB RAS," Opt. Atmos. Okeana **22** (10), 981−987 (2009).

40. F. Kasten, "Visibility forecast in the phase of precondensation," Tellus **21** (5), 631−635 (1969).

41. G. Hanel, "The properties of atmospheric aerosol particles as function of relative humidity at the thermody-

namic equilibrium with surrounding moist air," Adv. Geophys. **19**, 73−188 (1976).

42. Jr. Orr, C. F. K. Hurd, and W. J. Corbett, "Aerosol size and relative humidity," J. Colloid. Sci. **13** (5), 472−482 (1958).

43. I. N. Tang, "Phase transformation and growth of aerosol particles composed of mixed salts," J. Aerosol Sci. **7** (5), 361−371 (1976).

44. S. T. Martin, "Phase transitions of aqueous atmospheric particles," Chem. Rev. **100** (9), 3403−3453 (2000).

45. J. W. Fitzerald, "Approximation formulas for the equilibrium size of an aerosol particle as a function of its dry size and composition and the ambiant relative humidity," J. Appl. Meteorol. **14** (6), 1044−1049 (1975).

46. M. V. Panchenko, S. A. Terpugova, V. S. Kozlov, V. V. Pol'kin, and E. P. Yausheva, "Annual behavior of the condensation activity of submicron aerosol in the atmospheric surface layer of Western Siberia," Atmos. Ocean. Opt. **18** (8), 607−611 (2005).

47. S. A. Terpugova, M. V. Panchenko, M. A. Sviridenkov, and E. P. Yausheva, "Different types of dependence of aerosol properties upon relative humidity," J. Aerosol Sci. **1** (Suppl. 35), 1043−1044 (2004).

48. S. A. Terpugova, T. A. Dokukina, E. P. Yausheva, and M. V. Panchenko, "Seasonal peculiarities of manifestation of different types of gygrograms for the scattering coefficient," Opt. Atmos. Okeana **25** (11), 952−957 (2012).

49. V. A. Kovalev and W. E. Eichinger, *Elastic Lidar* (John Willey & Sons, Hoboken, New Jersey, 2004).

50. J. Ackermann, "The extinction-to-backscatter ratio of tropospheric aerosol: A numerical study," J. Atmos. Ocean. Technol. **15** (4), 1043−1050 (1998).

51. Yu. S. Balin, G. M. Krekov, I. V. Samokhvalov, and R. F. Rakhimov, "Humidity effect on the radar scatter-ing in the atmosphere," Meteorol. Gidrol., No. 8, 114−119 (1978).

52. G. de Leeuw, G. J. Kunz, and C. W. Lamberts, "Humidity effects on the backscatter/extinction ratio," Appl. Opt. **25** (22), 3971−3974 (1986).

53. T. L. Anderson, S. J. Masonis, D. S. Covert, R. J. Charlson, and M. J. Rood, "In situ measurement of the aerosol extinction to backscatter ratio at a polluted continental site," J. Geophys. Res. **105** (22), 26907−26915 (2000).

54. G. Feingold and B. Morley, "Aerosol hygroscopic properties as measured by lidar and comparison with in situ measurements," J. Geophys. Res., D **108** (11), 4327 (2003).

55. H. W. M. Salemink, J. B. Bergwerff, and P. Schotanus, "Quantitative lidar at 532 nm for vertical extinction profiles and the effect of relative humidity," Appl. Phys., B **34** (4), 187−189 (1984).

56. V. Wulfmeyer and G. Feingold, "On the relationship between relative humidity and particle backscattering coefficient in the marine boundary layer determined with differential absorption lidar," J. Geophys. Res., D **105** (4), 4729−4741 (2000).

57. E. Dupont, J. Pelon, and C. Flamant, "Study of the moist convective boundary layer structure by backscattering lidar," Bound.-Lay. Meteorol. **69** (1), 1−25 (1994).

58. World Meteorological Organization. Guide to meteorological instruments and methods. No. 8 (2008). http://www.wmo.int/pages/prog/www/IMOP/CIMO-Guide.html/.

59. http://loza.iao.ru.

Translated by O. Bazhenov